Implications of high-resolution velocity and strain rate observations for modelling of Greenlandic tidewater glaciers

Dominik Fahrner[1,2]*, Pablo J. González[3,4]*, Douglas W. F. Mair[1] and James M. Lea[1]

[1]Department of Geography and Planning, University of Liverpool, Liverpool, UK; [2]Department of Glaciology and Climate, Geological Survey of Denmark and Greenland, Copenhagen, Denmark; [3]Department of Earth, Ocean and Ecological Sciences, COMET, University of Liverpool, Liverpool, UK and [4]Department of Life and Earth Sciences, Volcanology Research Group, Institute of Natural Products and Agrobiology, Spanish National Research Council (CSIC), La Laguna, Spain

Abstract

Synthetic Aperture Radar (SAR) has been used extensively to determine the surface ice flow velocity of tidewater glaciers and investigate changes in seasonal or annual ice dynamics at medium spatial resolution ($\geqslant 100$ m). However, assessing tidewater glacier behaviour at these resolutions risks missing key details of glacier dynamics, which is particularly important for determination of strain rates that relate to crevasse formation, depth, and ice damage. Here we present surface ice velocity and strain maps with a 16 m posting derived from high-resolution (1 m) PAZ Ciencia spotlight mode SAR imagery for Narsap Sermia, SW Greenland, for October 2019 to February 2021. Results reveal fine details in strain rate, including an area of compression proximal to the terminus, with an upstream shift of strains through time. The velocity evolution of Narsap Sermia shows distinct seasonal changes starting in summer 2020, which are largely modulated by the subglacial drainage system. Comparison of our results with medium-resolution velocity products shows that while these can capture general strain and velocity patterns, our high-resolution data reveals considerably larger ranges of strain values. This is likely to have implications for tuning strain rate dependent calving and ice damage parameterisations within numerical models.

Introduction

Synthetic Aperture Radar (SAR) data has been widely used to determine flow velocities and stress/strain fields for understanding the dynamics of fast flowing Greenlandic outlet glaciers (Joughin and others, 1996; Strozzi and others, 2002; Rignot and Kanagaratnam, 2006; Moon and others, 2012, 2014; Nagler and others, 2015; Riel and others, 2021). SAR imagery is often favoured over optical imagery to investigate tidewater glacier dynamics as it is unaffected by cloud conditions allowing more spatio-temporally continuous data acquisition, with typical posting resolutions of 100–500 m (Mouginot and others, 2019; Solgaard and Kusk, 2019). These posting resolutions of the velocity and strain fields are a function of the true resolution of the underlying SAR image and size of the estimation window required during velocity and strain processing estimation (Howat and others, 2005; Joughin and others, 2008, 2018; Rohner and others, 2019). Though data acquired by SAR platforms with higher true-resolution offer the opportunity to acquire more spatially detailed insights into tidewater glacier dynamics.

Velocity data are frequently used to underpin the investigation of tidewater glacier (TWG) dynamics, initial inputs for numerical models, and derivation of key parameters that form part of simulations. For example, glacier velocity observations have previously been used to determine ice deformation within glaciers, their basal conditions, and assess changes in their behaviour (Knight, 1992; Mair and others, 2002a, 2002b; Luckman and Murray, 2005; MacGregor and others, 2016). As part of this, the derivation of strain rate from velocity provides information relating to ice damage, crevasse formation and depth which has potential to significantly impact calving behaviour of TWGs (Weertman, 1973; van der Veen, 1998; Benn and others, 2007a, 2007b; Cowton and others, 2019). Given that the calculation of strain rate requires spatially distributed velocity observations at a single point in time, the potential length scales of strain rate data are directly limited by the spatial resolution of velocity data. Higher resolution velocity data therefore offers the potential for exploring strain rate variability at shorter length scales, providing greater insight into finer scale variability of ice flow.

The calving of tidewater glaciers is influenced by processes that operate at a large range of spatial scales, yet strain rate has been suggested to be a first-order control (Benn and others, 2007a, 2007b; Borstad and others, 2012, 2013). Strain rate further directly influences the initialisation and evolution of ice damage fields and crevasse formation, which are of particular importance for iceberg calving parameterisations (e.g. Choi and others, 2021). This highlights the relevance of determining correct magnitudes of local strain rate, as underestimates of these parameters could have potentially substantial impact on the results of prognostic simulations.

Depending on the type of numerical model and set-up, the spatial resolution of these simulations for calving glaciers typically varies on the order of 10^1–10^2 m, while the resolution of

velocity observations currently limit the resolution of strain rate data to several hundred metres. Consequently, the current spatial resolution of strain rate observations derived from velocity data of the order of 10^2 m scale may obscure finer scale processes that are of importance for tuning of parameters for model initialisation, spin up, and forward simulations.

In this study, focussing on Narsap Sermia between October 2019 and February 2021, we compare the analysis of velocities and strain rates using PAZ data to TerraSAR-X derived MEaSUREs data (Joughin and others, 2010, 2021), to evaluate if current medium-resolution data are able to capture velocity and strain extrema accurately. We further discuss the potential of using high-resolution PAZ spotlight mode SAR data (~1 m pixel resolution of raw data) to improve the spatial resolution of glacier flow velocities, shear, and longitudinal strain rates by up to a factor of five.

Data and methods

Site description

Narsap Sermia is a tidewater glacier in SW Greenland that has largely been stable since the Little Ice Age (at least since 1855) but has experienced a significant speed up from 1.5 to 5.5 km a^{-1} and retreat of ~5 km since 2005 (Weidick, 1959; Motyka and others, 2017; Davison and others, 2020; Fahrner and others, 2021). The glacier terminus is retreating towards an overdeepening in the bedrock topography of approximately 400 m which, once the terminus reaches the reverse slope, could lead to an increase in ice discharge, iceberg size and its rapid retreat (Schoof, 2007; Morlighem and others, 2017, 2021; Van Wyk de Vries and others, 2023). Since at least 2014, when seasonal velocity analysis became possible, Narsap Sermia has exhibited distinct phases of spring acceleration, midsummer slowdowns and winter recovery, which are modulated by subglacial runoff and the evolution of the subglacial hydrological system (Davison and others, 2020).

Data

We use PAZ Ciencia spotlight mode Synthetic Aperture Radar data acquired between 30/10/2019 and 23/02/2021 with an 11-day revisit time, providing a total of 43 images. We derive 42 velocity maps using a daisy-chain approach (i.e. displacement between image 1 and image 2, displacement between image 2 and image 3, etc). The satellite is tasked to acquire data for a 12 km by 12 km area of interest (Fig. 1, turquoise box) in descending orbit with single polarisation and an incidence angle of ~32° at the centre of the scene. Spotlight mode was favoured as it can achieve a higher azimuth resolution and subsequently a higher overall spatial resolution (azimuth and range directions of 1.1 and 1.2 m; (HDS Team, 2019)). Data are delivered in single-look complex image format, and an ASTER DEM is automatically downloaded and subsequently up-sampled using an 2 m ArcticDEM strip for georeferencing.

Methods

Velocity

The Single Look Complex (SLC) spotlight mode data are processed using the open-source InSAR Scientific Computing Environment 2.2.0 (ISCE; Rosen and others, 2012) and, due to similar SLC data formatting and viewing geometries, we can apply the TerraSAR-X stripmap mode processing chain without modifications. To derive velocities, offsets between consecutive image pairs are computed through normalised cross correlation using the Ampcor module, and geocoded with a window width of 256 pixels, a search width of 88 pixels and a skip width of 30 pixels. These parameters are determined to be most suitable, based on velocities calculated in previous studies for Narsap Sermia (e.g. Motyka and others, 2017; Davison and others, 2020), to capture pixel offsets between image pairs upstream of the terminus accurately.

As this study is looking at horizontal (i.e. surface parallel) velocities only, we assume no movement in the vertical direction (Moon and others, 2014, 2015). Range offsets are sensitive to satellite to ground line-of-sight motion, which is quite steep (34-degree incidence angle) and hence sensitive to vertical motion. However, surface elevation changes at Narsap Sermia range between −2.6 and −6.3 m a^{-1} (2016 to 2018) and thus can be considered negligible as they are several orders of magnitude smaller (max $\Delta h < 0.073$ m per 11 days) than the resulting velocities (Studinger, 2014). The azimuth and range offsets are converted from radar coordinate pixel-spacing to geographic pixel-spacing by multiplication with the azimuth and range spacing (~1 m) to retrieve a pixel-posting of 16 m and an underlying true spatial resolution of 256 m. The resulting values are further transformed to East-West/North-South and flow parallel/perpendicular direction using 2-D vector rotation. For the rotation to flow parallel/perpendicular, we assume a flow direction of −135° measured from North for Narsap Sermia (with positive degree values to the West). The velocity magnitude is calculated, and a band-pass pass filter is applied to remove potential outliers (excluding top and bottom 0.5% of observations).

Velocities at the terminus and up to ~3 km upstream could not be captured, most likely due to the influence of changing mélange and near-terminus ice being calved between revisit times (Fig. S1). It was possible to identify these spurious velocities visually by (i) the presence of large velocity gradients between individual pixels, which is more associated with the movement of mélange (Amundson and others, 2010; Sutherland and others, 2014); and (ii) areas where flow velocities show unrealistic values of ≫1000 m d^{-1} (Fig. S1). The identified areas of erroneous velocities have been masked out in grey on subsequent maps and figures and are excluded from the analysis.

Stacked median velocity and strain rate maps were created to provide an overview of the data, with the median being calculated using the cell statistics tool within ArcMap 10.7 (Figs 2, 6, S2). The stacked maps make it possible to identify areas of consistent high/low velocity and strain, which allows to put surface dynamics in relation to the underlying bedrock topography.

To show spatial differences in velocities over time, individual velocity maps for the period 12/4/2020 to 23/01/2021 were subtracted from the mean of the period 30/10/2019–01/04/2020, as this period showed relatively little variability and was thus considered to represent background winter velocities (Sole and others, 2013; Tedstone and others, 2015; Bartholomaus and others, 2016).

Strain rate

Longitudinal, transverse and shear strain rates ($\dot{\varepsilon}_{xx}$, $\dot{\varepsilon}_{yy}$, $\dot{\varepsilon}_{xy}$) were calculated using the x and y velocity vectors which have previously been derived from azimuth and range offsets (posting 16 m). At its finest resolution, mean flow direction is calculated by taking data from 80×80 m blocks (5×5 pixels), before strain rate is calculated over a 48×48 m (3 by 3 pixels) sub-grid that is orientated ice flow parallel, with velocity values for each sub-gridpoint obtained through bilinear interpolation. The strain rate values calculated over the sub-grid are stored in a matrix $S_{i,j}$ with i rows and j columns, with the subscript indicating the position of the value within the sub-grid and the velocity vector
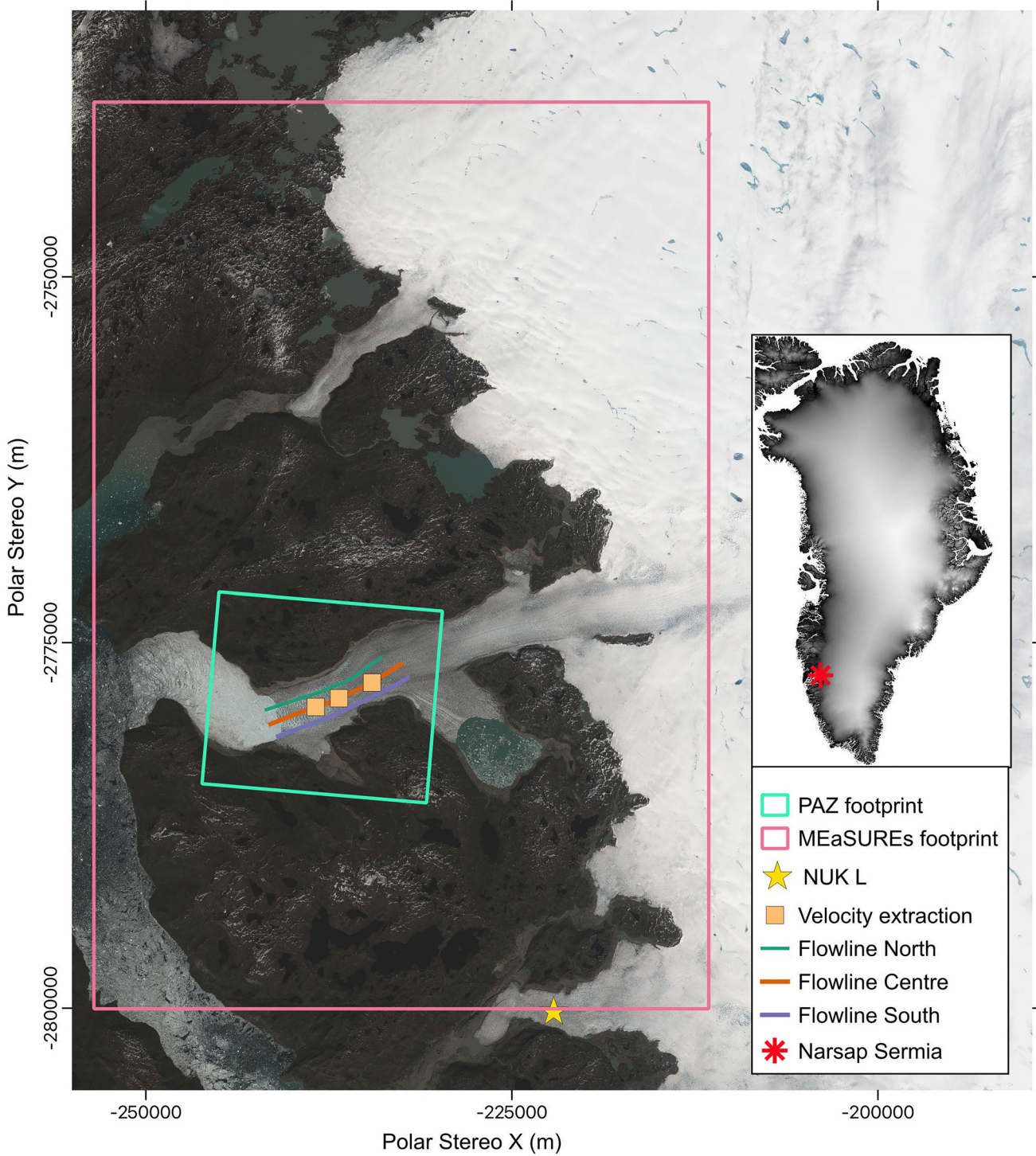
Figure 1. Footprint of acquired PAZ Satellite Aperture Radar data (pink) and MEaSUREs Satellite Aperture Radar data (turquoise; Joughin and others, 2010, 2021) on top of Mosaic of European Space Agency (ESA) Sentinel-2 RGB images acquired on 09/07/2021. Inset map shows location of Narsap Sermia (red cross) on top of surface topography from BedMachine V4 (Morlighem and others, 2017, 2021).

used (x or y velocity vectors). Longitudinal ($\dot{\varepsilon}_{xx}$), transverse ($\dot{\varepsilon}_{yy}$) and shear ($\dot{\varepsilon}_{xy}$) strain rates are then calculated as shown in Eqns (1)–(5).

$$\dot{\varepsilon}_{xx} = \frac{\sum\left(\frac{S_{1,2,x} - S_{1,1,x}}{x} \cdots \frac{S_{3,3,x} - S_{3,2,x}}{x}\right)}{n} \quad (1)$$

$$\dot{\varepsilon}_{yy} = \frac{\sum\left(\frac{S_{1,2,y} - S_{1,1,y}}{y} \cdots \frac{S_{3,3,y} - S_{3,2,y}}{y}\right)}{n} \quad (2)$$

$$A = \frac{S_{3,2,x} - S_{2,2,x}}{y}, \quad \frac{S_{2,2,x} - S_{1,2,x}}{y} \quad (3)$$

$$B = \frac{S_{2,3,y} - S_{2,2,y}}{x}, \quad \frac{S_{2,2,y} - S_{2,1,y}}{x} \quad (4)$$

$$\dot{\varepsilon}_{xy} = \frac{\frac{\sum(A)}{\sum(A \in \{0, 1\})} + \frac{\sum(B)}{\sum(B \in \{0, 1\})}}{2} \quad (5)$$

Table 1. Available MEaSUREs v.4 velocities derived from SAR data and the time interval in days between individual data products

Dates of available SAR image pairs	Time interval (d)
12/11–23/11/2019	55
06/01–17/01/2020	110
25/04–06/05/2020	88
22/07–02/08/2020	187
25/01–02/05/2021	–

With *n* being the number of grid points and A∈{0,1}, B∈{0,1} being the conversion of A and B to logical values.

The PAZ derived strain rates were compared to strain rates derived from the National Snow & Ice Data Centre's (NSIDC) MEaSUREs version 4 velocities for the period 12/11/2019 to 02/05/2021 as an example of currently existing velocity data products (Joughin and others, 2010, 2021). In order to compare both data products, PAZ x and y velocities are recalculated to metres per year and reprojected to the polar stereographic grid. MEaSUREs x and y velocities, which are derived from TerraSAR-X/TanDEM-X SAR image pairs with an 11-day time difference between acquisitions, have a true resolution of several hundred metres and a posting of 100 m. The frequency of available MEaSUREs velocity products varies between a minimum of 55 days and a maximum of 187 days between sets of image pairs (Table 1).

Time series and outlier identification

Potential outlier pixels containing incorrect strains or velocities within the mélange are excluded by cropping the resulting maps using ice masks derived from tracing the glacier extent from each individual geocoded SAR image. Each SAR image is geolocated by co-registering all SAR images to the same PAZ reference image (image: 30/10/2019). The final mask used for each velocity acquisition is determined from whichever of the two masks from each image pair covered the smallest glacier extent.

Velocity values are extracted along a centreline and at 3.3, 5 and 7.5 km on the centreline, which have been determined to be locations with the least data gaps, to better visualise flow variability over time (Figs 1, S2). Strain rates are extracted along the centreline to enable the comparison between PAZ And MEaSUREs data (Fig. 2), and along lines in the northern, central, and southern sectors of the glacier to facilitate the analysis of PAZ derived strain rates through time (Figs 1, 6).

Bedrock topography is extracted for each line from BedMachine v4 with corresponding error estimates (Morlighem and others, 2017, 2021).

Terminus position and climate

Termini are digitised for each PAZ SAR image (Fig. S3) and margin change is quantified using the curvilinear box method within the Margin Change Quantification Tool (MaQiT; Lea, 2018), with a box width equal to the width of the terminus (3200 m).

Air temperature data are taken from a PROMICE weather station (NUK_L), positioned on Qamanaarsuup Sermia approximately 25 km to the southeast from the centreline of Narsap Sermia at an elevation of 530 m a.s.l. (Fig. 1; Fausto and Van As, 2019).

Runoff is extracted and summed for the catchment of Narsap Sermia from daily MAR v3.11.2 (Modèle Atmosphérique Régional) data with a 6 km resolution (Fig. S4; Fettweis and others, 2017; Mouginot and Rignot, 2019; Colosio and others, 2021). The MAR data do not account for subglacial runoff storage

or transit times, therefore subsequent analysis assumes instantaneous runoff of meltwater.

Results

Comparison of PAZ and MEaSUREs SAR data

Figure 2 shows the comparison of shear and longitudinal strain rates derived from MEaSUREs and PAZ SAR data, which have been calculated over their respective velocity data postings of 100 and 16 m respectively.

The stacked shear and longitudinal strain rate maps show that both data products capture similar spatial patterns, but also reveal clear differences in the spatial distribution of strain rates (Figs 2a, b, e, f). For longitudinal strain rates, the spatial differences are most distinct at the margins, where PAZ data reveals an area of compression in the southern sector, whereas MEaSUREs data indicates close to zero strain rates. Spatial differences in shear strain rates are most apparent in the centre of the glacier, with PAZ indicating branches of left- and right-lateral shear towards the glacier centre (at ∼3 and 6 km from the terminus), while the coarser resolution of the MEaSUREs data does not allow similar features to be identified. The differences are also apparent from the values extracted along the centreline transects, with local variations in strain rates in the PAZ data not being resolved by the MEaSUREs data.

The comparison of longitudinal strain rates between MEaSUREs and PAZ data shows that the overall patterns of extension (positive values) occur in similar locations for the entire observation period (Figs 2d, h). However, areas of compression (negative values) at ∼2.5 and ∼8 km from the terminus that are identified in the PAZ data are not resolved in the MEaSUREs data (Figs 2d, h). It is apparent that the higher spatial resolution PAZ data enables the identification of localised variability in strain rate that are not resolved in the MEaSUREs data.

Areas of right-lateral shear at ∼3 and ∼6 km from the terminus are more apparent in the transects of the PAZ data compared to MEaSUREs (Figs 2g, h). The high-resolution PAZ data are further able to capture considerably more complex distributions of shear strain rates along the flowline, with a zone of low right-lateral shear branching out across the glacier at ∼7.5 km from the terminus (Fig. 2g).

To illustrate how pixel-posting level impacts both the level of detail and values of strain rate derived, Figure 3 shows a longitudinal strain rate map of a PAZ velocity data acquisition (30/10/2019 to 11/11/2019) that has been continuously down sampled from its original resolution (16 m posting) to the MEaSUREs resolution (100 m posting). This highlights that 100 m resolution data generalises areas of compression and extension where those are the dominant signal, while high-resolution data reveal a much more complex pattern of local strain rate variability. As posting level becomes finer, the range of strain rate values is also found to increase substantially (Figs 2, 3).

Velocity evolution from PAZ data

The velocities derived from PAZ spotlight mode data show a general pattern of high velocities close to the terminus (∼25 m d^{-1}) and gradually decreasing velocities upstream (∼5 m d^{-1} at 10 km from terminus; Figure 4). The velocity evolution of Narsap Sermia over the study period can be qualitatively categorised in four different stages (Fig. 4a):

Stage 1 (30/10/2019–12/4/2020): Velocities remain steady from the start of the observational period in October 2019 until the beginning of April 2020, coinciding with a period where runoff is minimal or absent and air temperatures are below zero degrees.
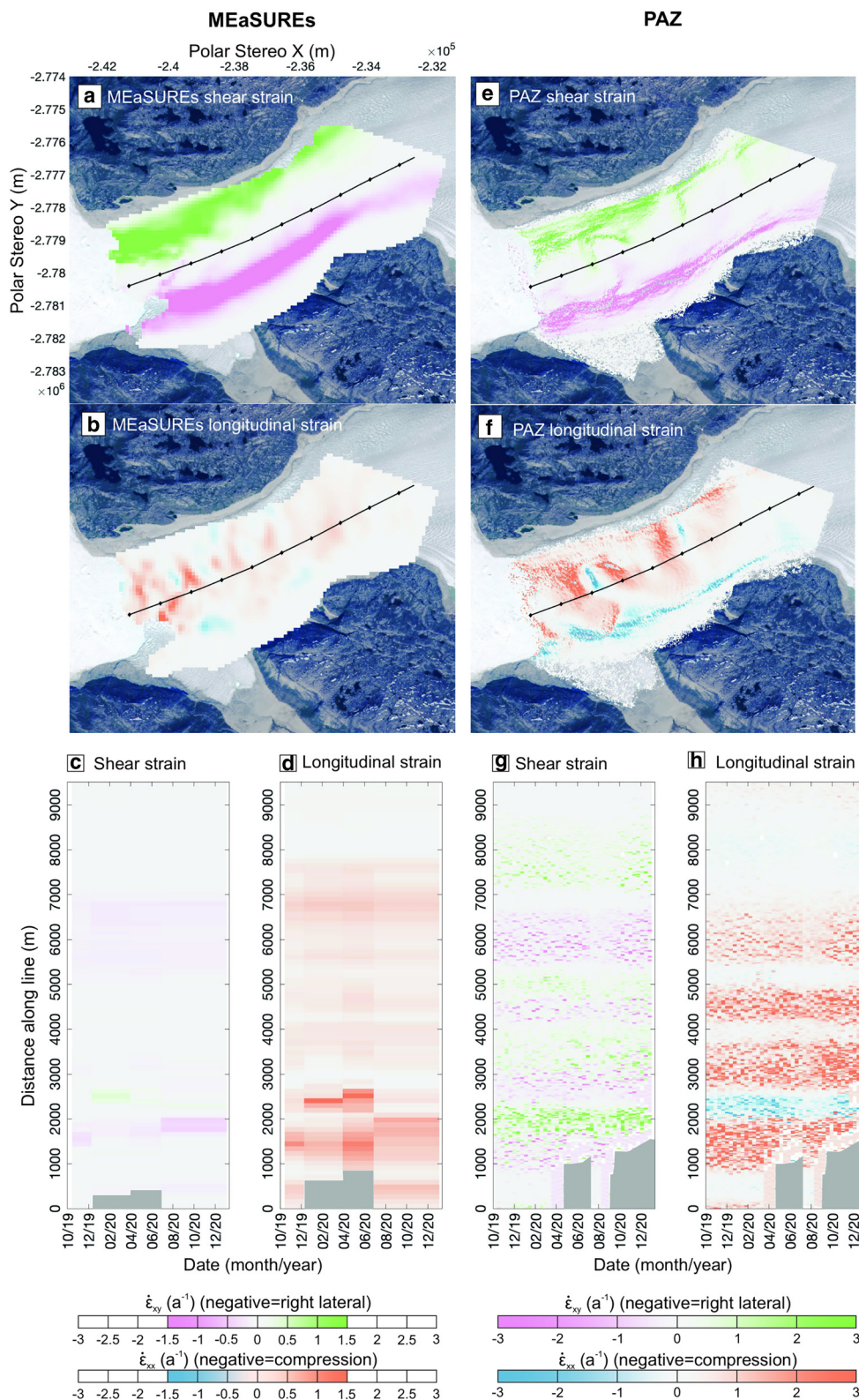
Figure 2. Comparison of shear and longitudinal strains derived from MEaSUREs SAR data (a–d) and PAZ SAR data (e–h) along the centreline with black ticks marking 1 km segments. Centrelines for MEaSUREs and PAZ data are shown in panels a, b and e, f respectively on top of stacked (median) shear and longitudinal strain rate maps (MEaSUREs strain rate posting is 100 m, PAZ strain rate posting is ~16 m). Basemaps show an ESA Sentinel-2 RGB image, acquired on 09/07/2021. NOTE: MEaSUREs data are shown with a different range. No-data areas are shown in light grey.

The terminus position remains stable from the start of the observation in October 2019 until January 2020, followed by an advance of ~200 m until mid-March and subsequent retreat of ~120 m until the end of Stage 1 (12 April 2020).

Stage 2 (12/04/2020–31/7/2020): This stage coincides with the initiation of runoff, where an increase in flow velocities is observed, with the magnitude of this acceleration decreasing with distance from the glacier terminus ([Figs 4a, c](#)). Velocities reach their maximum in mid-May with speeds of ~22 m d^{-1} close to the terminus and ~10 m d^{-1} further upstream. This stage is characterised by positive air temperatures, with 92 out of 110 days experiencing temperatures >0°C (Fig. S5) at NUK_L
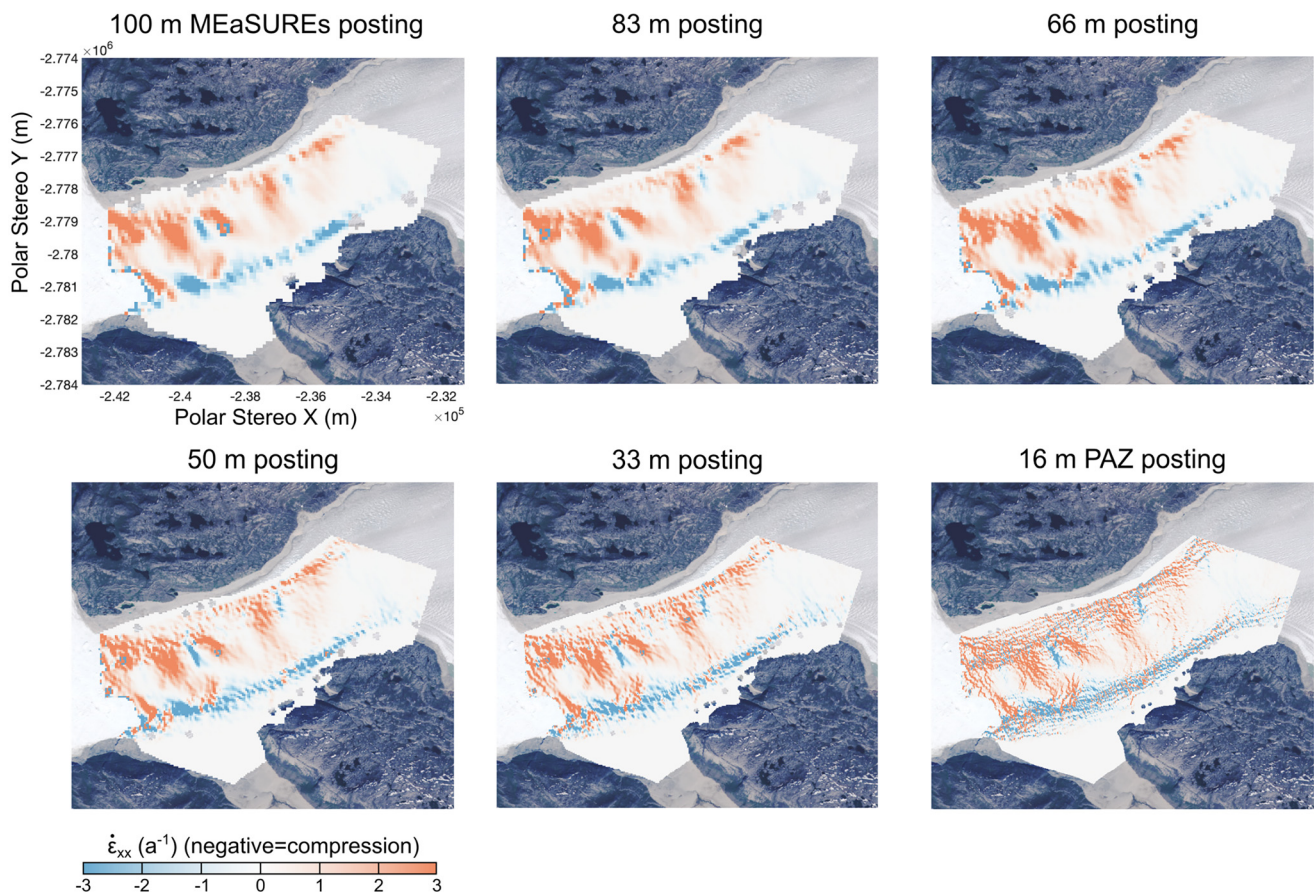
Figure 3. PAZ SAR derived longitudinal strain rates (derived from image pair from 30/10/2019 and 11/11/2019) processed at different postings to highlight the difference between MEaSUREs data posting (100 m) and PAZ data posting (~16 m). Basemap shows an ESA Sentinel-2 RGB image, acquired on 09/07/2021.

weather station and runoff peaks in June and July. During this stage there is an overall terminus retreat of 550 m, punctuated by two small re-advances of ~50 m and ~16 m during the periods 4/05–15/05 and 17/06–28/06, respectively (Figs 4a, e).

Stage 3 (31/07/2020–11/08/2020): During this 11 day period a clear velocity slowdown is apparent, which is most pronounced at 3.3 km from the terminus (magnitude of deceleration ~7 m d^{-1}) but can also be observed further upstream (~6 m d^{-1} at 5 km; ~5 m d^{-1} at 7.5 km; Figure 4c).

Stage 4 (11/08/2020–02/02/2021): Starting in mid-August, velocities gradually increase until the end of the observation period in February 2021. Runoff only occurs at the start of the stage and air temperatures begin to decrease with only 49 out of 154 days showing temperatures above 0°C (Fig. S5). Terminus retreat is apparent between 02/09 and 27/10 (~420 m), followed by relative stability and overall slight advance (~25 m) from 17/10 until the end of the observation period.

To illustrate the spatio-temporal patterns of velocity change, Figure 5 shows the differences between mean Stage 1 velocities (Fig. S2), and those of Stages 2 – 4. In Stage 2, velocity anomalies are initially high in the northern sector of the glacier and low in the southern sector of the glacier (12/04–23/04). This state is subsequently reversed, and velocities start to considerably increase from the southern sector of the glacier, with maximum velocity anomalies of >8 m d^{-1} being reached at the terminus. Negative velocity anomalies are however apparent in the northern sector along the lateral ice-bedrock border. The summer slow-down (Stage 3) is clearly apparent across the study area, with velocity anomalies being up to ~8 m d^{-1} lower than during Stage 2 and up to ~4 m d^{-1} lower than mean winter velocities (Stage 1). The onset of a positive velocity anomaly can be seen in the

northern sector of the terminus at the beginning of Stage 4 (11/ 08/ – 22/08/2020), which subsequently propagates ~1 km upstream (02/09/2020) before spreading laterally across the glacier. By mid-September (13/09/2020), increased velocities reach the southern part of the terminus and encompass most of the near-terminus area. While it can be assumed that increased velocities are present in the near-terminus area, data gaps prevent definitively determining the extent of the acceleration close to the terminus (Fig. 5, Stage 4). The positive velocity anomalies propagate further upstream over time, so that increased velocities are apparent across the study area by the end of the observation period (03/02/2021). The data gaps increase in spatial extent over the period 22/08/2020 – 03/02/2021, which substantially limits the analysis of the acceleration between the terminus and ~3 km upstream.

Spatio-temporal strain rate evolution

There is a distinct separation between longitudinal strain rates in the northern and southern part of the glacier, with extension (i.e. longitudinal stretching; positive values) dominating in the central and northern sectors of the glacier (Figs 6c–e), and compression (negative values) being dominant in the southern sector of the glacier.

Extension in the northern sector is present near-terminus, and at ~3, 4.5 and 6.5 km from the terminus (Fig. 6c, *ii–iv*). A small area of compression is apparent at the start of an over-deepening (at ~7 km from the terminus) that extends further inland to a depth of ~400 m. Bedrock topography data along the flowline from BedMachine v4 suggests that subglacial topography is relatively flat at the terminus but shows local reverse bed slopes at
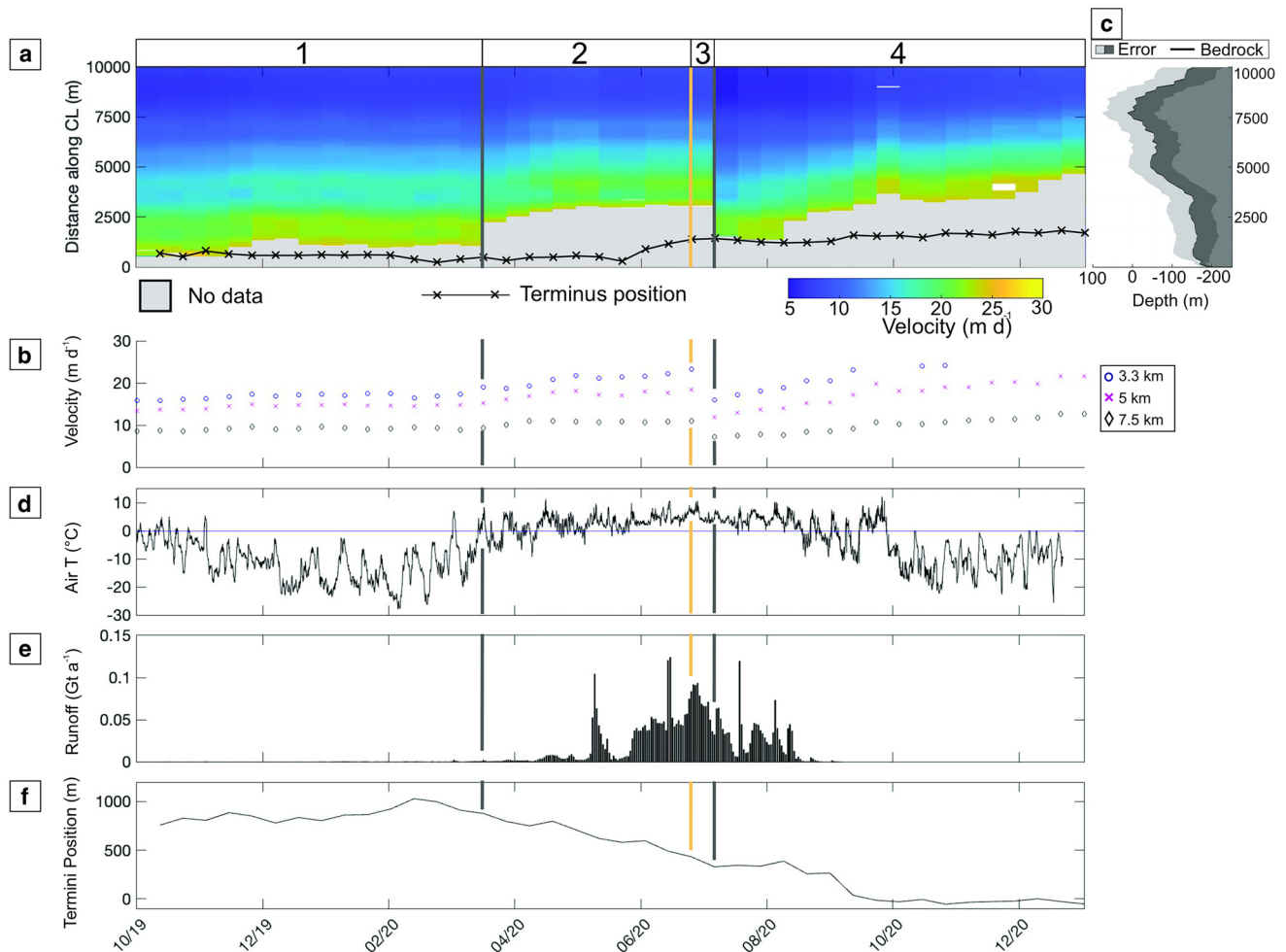
Figure 4. Velocity evolution over time (30/20/2019 – 23/01/2021) from high-resolution PAZ SAR data (a) along the centreline with terminus position at the centreline shown in black and no data areas masked out in grey. (b) Velocities from points at 3.3 (circle), 5 (cross) and 7.5 km (diamond), respectively (Points shown in Fig. 1). (c) bedrock topography and errors extracted along the centreline from BedMachine v.4 data (Morlighem and others, 2017, 2021). (d) Air temperature from the PROMICE weather station NUK L, approximately 25 km to the southeast of Narsap Sermia. (e) Daily runoff for the Narsap Sermia catchment extract from MAR v3.11.2 (Mouginot and Rignot, 2019; Colosio and others, 2021). (f) Terminus position relative to the most recent observation computed in MaQiT. Yellow line shows start of the midsummer velocity slowdown.

~3, 5 and 7 km from the terminus where we find extensional strain (Fig. 6c; Morlighem and others, 2017, 2021).

In the centre, we find four distinct bands of extensional strain rates at ~2, 3.5, 5, and 6 km from the terminus with their magnitudes decreasing with distance from the terminus (Fig. 6d, v–viii). Extensional strain rates are apparent on flat (Fig. 6d, v & vii) as well as reverse bed slopes (Fig. 6d, vi & viii).

In the southern sector (Fig. 6e), compressional strain rates are slightly more dominant in the first 2 km from the terminus, followed by intermittent bands off extension and compression up to 5.5 km from the terminus. Between ~5.5 and 9 km from the terminus we find a sector of high compressional strain rates, which coincides with a rise in local topography to ~100 m a.s.l. (Fig. 6e, x). An area of compression, which is apparent close to the terminus could correspond to the ice flowing over a small shallow trough (Figs 6a, b, e – dashed box). However, data gaps prevent tracking the evolution of the area of compression over the study period.

The evolution of strain rates shows little spatial variation over time (i.e. changes in sign of strain rate). In the south, strains are more compressional, though extensional strain values are also present whereas in the north and centre, extensional strains are more dominant (Figs 6c, d, e). Shear and transverse strains did not reveal any distinct spatial patterns or changes over time

(Fig. S6). However, in the southern part of the glacier, bands of high left-lateral shear strain are apparent between 8 and 10 km from the terminus. This coincides with BedMachine v4 data suggesting that the bedrock topography is well above sea level (~100 m a.s.l.) and starting to slope in the direction of ice flow (Figs S6, 6).

Discussion

Comparison of PAZ SAR data with MEaSUREs resolution

The comparison of high-resolution PAZ SAR derived strain rates to MEaSUREs derived strain rates shows that the latter provide a general overview of the strain regimes but clearly simplify the spatial patterns of surface strain rates (Fig. 2). The results further reveal a difference in the range of surface strain rate values with higher values being derived from PAZ data.

The kernel density estimation (KDE) plot in Figure 7a shows that medium-resolution data can capture broadly similar strain rate distributions for a given area of interest (Fig. 7d). However, it is quite apparent that strain rate extremes, which are highlighted in Figures 7b, c by applying a manually set (exclude values between −3 and 3) and quantiles based (25/75%) bandpass filter, are not captured by medium-resolution data. This provides a
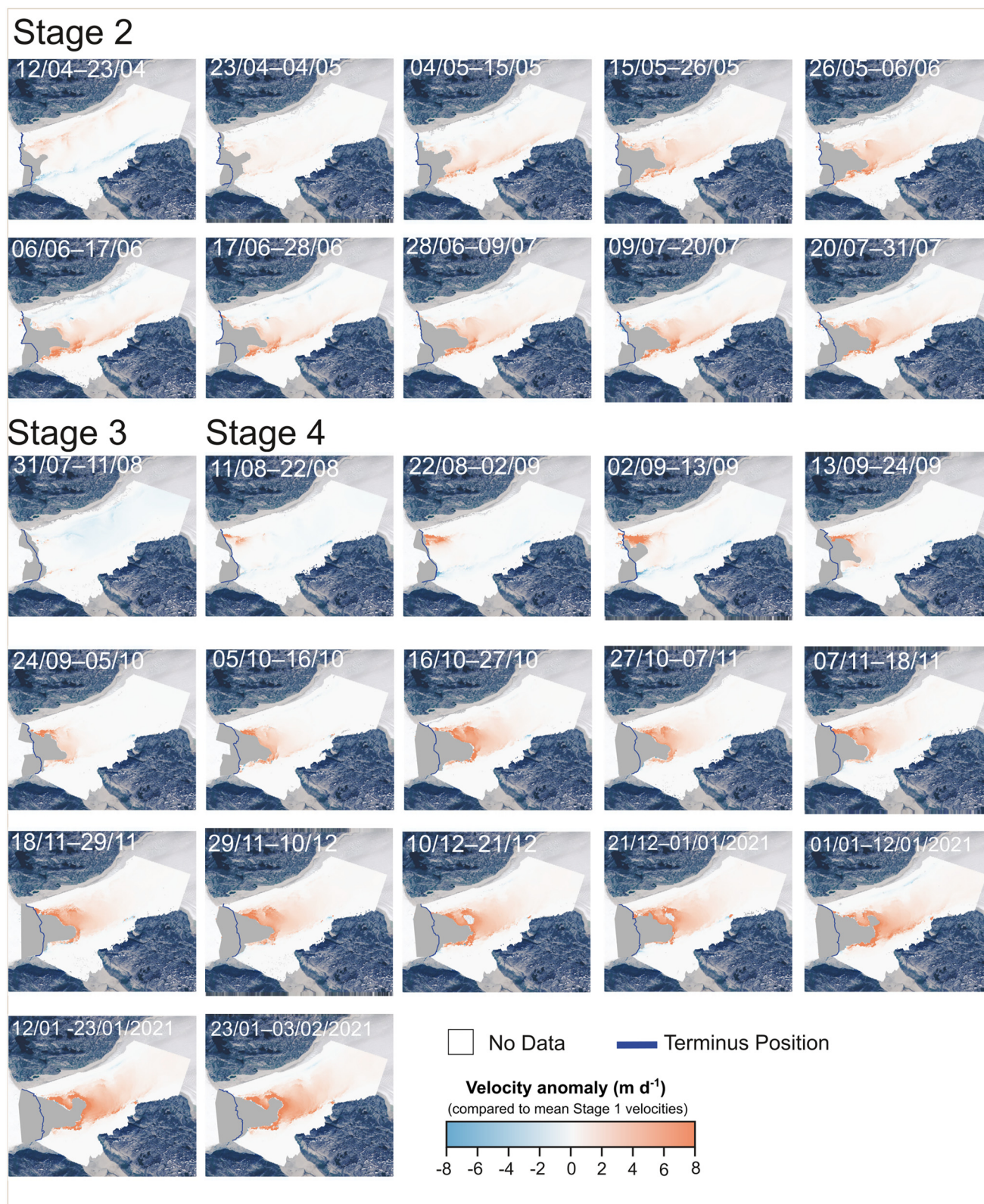
Figure 5. Difference of velocities of Stages 2–4 to the mean of Stage 1 (for Stages see Fig. 4) with data gaps masked out in grey and terminus positions shown as blue lines. Basemap shows an ESA Sentinel-2 RGB image acquired on 09/07/2021.

demonstration that coarser resolution data are likely to underestimate the magnitude of surface strain rates, especially for positive strain rates. For the cases shown in Figures 7b and c, positive strain rate distribution peaks identified in the high-resolution data are approx. 28 and 40% higher respectively, compared to data products with lower spatial resolution (Figs 2, 3; Rohner and others, 2019).

Implications for calving, ice damage and implementation in ice sheet models

Our results confirm that obtaining strain rates from medium-resolution MEaSUREs data (length scales of 300 m) compared to finer scale PAZ data (length scales of 48 m) lead to a more smoothed impression of surface ice velocity which is not
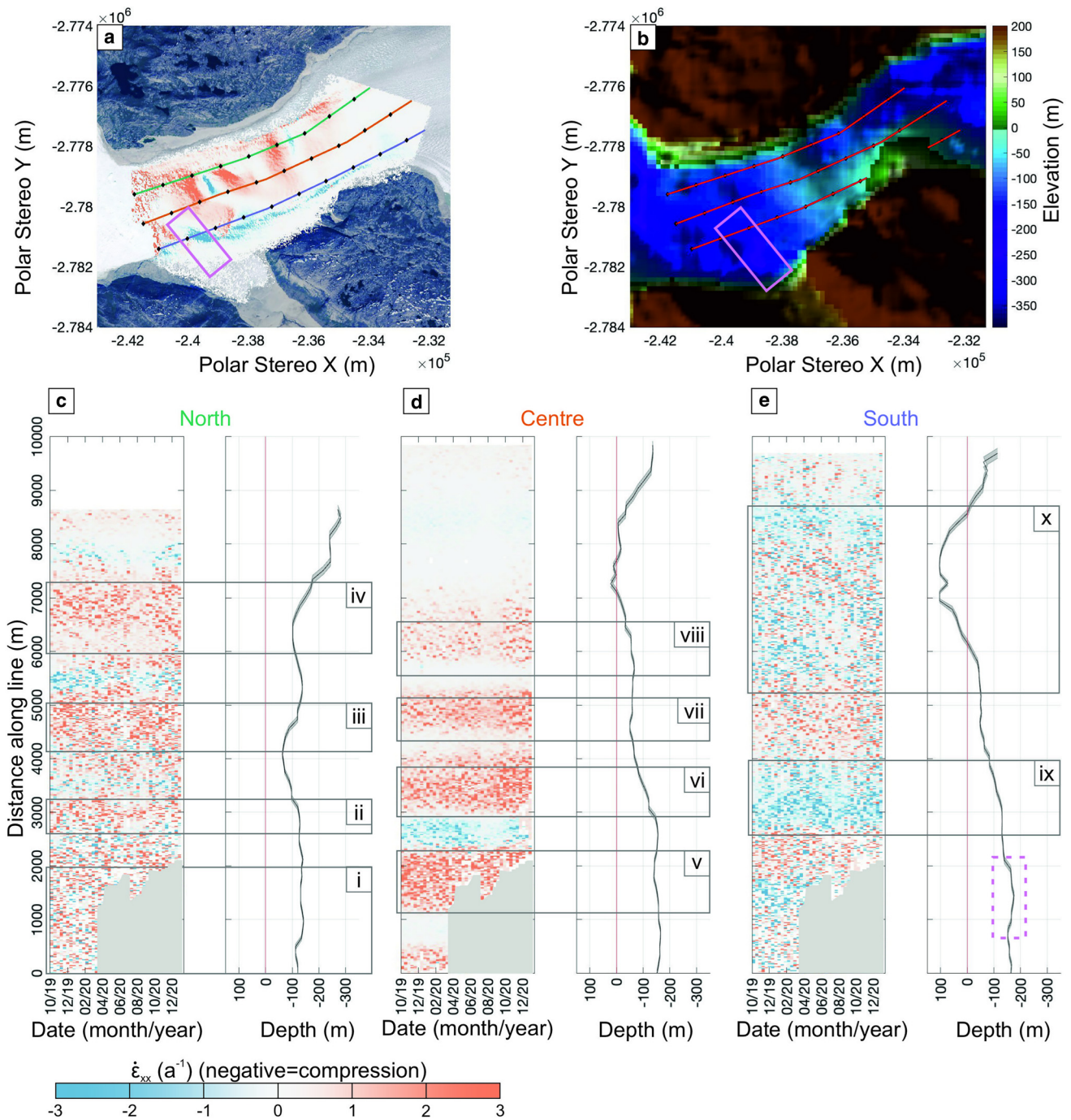
Figure 6. (a) Stacked longitudinal strains (median) with basemap showing an ESA Sentinel-2 RGB image, acquired on 09/07/2021. Location of strain extraction lines shown for the northern sector (green), the central sector (yellow) and the southern sector (light purple), black ticks marking 1 km segments, and location of small trough shown as purple rectangle. (b) Bedrock topography map (BedMachine v.4; Morlighem and others, 2017, 2021) with value extraction lines shown in red, black ticks marking 1 km segments, and location of small through shown as purple rectangle. (c–e) Temporal evolution of longitudinal strains for northern, central, and southern sector with corresponding bedrock topography and error (grey shaded). Boxes i–x show location of high strain, light pink dashed box shows location of small shelf and shallow through. No data areas are shown in light grey.

representative of TWG behaviour at length scales over which crevasses typically form (Borstad and others, 2012; Rohner and others, 2019). When constraining calving behaviour and ice flow in current ice sheet models, using strain rates derived from modelled or observed velocities with coarser posting levels (i.e. the order of 10^2 m) could result in the underestimation of key parameters such as ice damage, crevasse formation rates, crevasse depths, and the enhancement factor E (Borstad and others, 2012; Larour and others, 2012; Morlighem and others, 2016; Rohner and others, 2019). These parameters are especially relevant in calving and diagnostic models, which aim to enhance our process

understanding of calving behaviour, crevasse formation and ice damage evolution. For example, inverting for ice damage and in turn the enhancement factor E directly from medium-resolution velocity observations or model output could lead to an underestimation of both parameters thereby suggesting that higher stresses are required for calving to occur (e.g. Borstad and others, 2013). Consequently, model simulations that are tuned to fit observations through basal inversions may be doing so by overestimating values of the basal sliding parameter.

For both calving and ice damage parameterisations within process level model simulations performed at grid scales of $<10^2$ m^2,
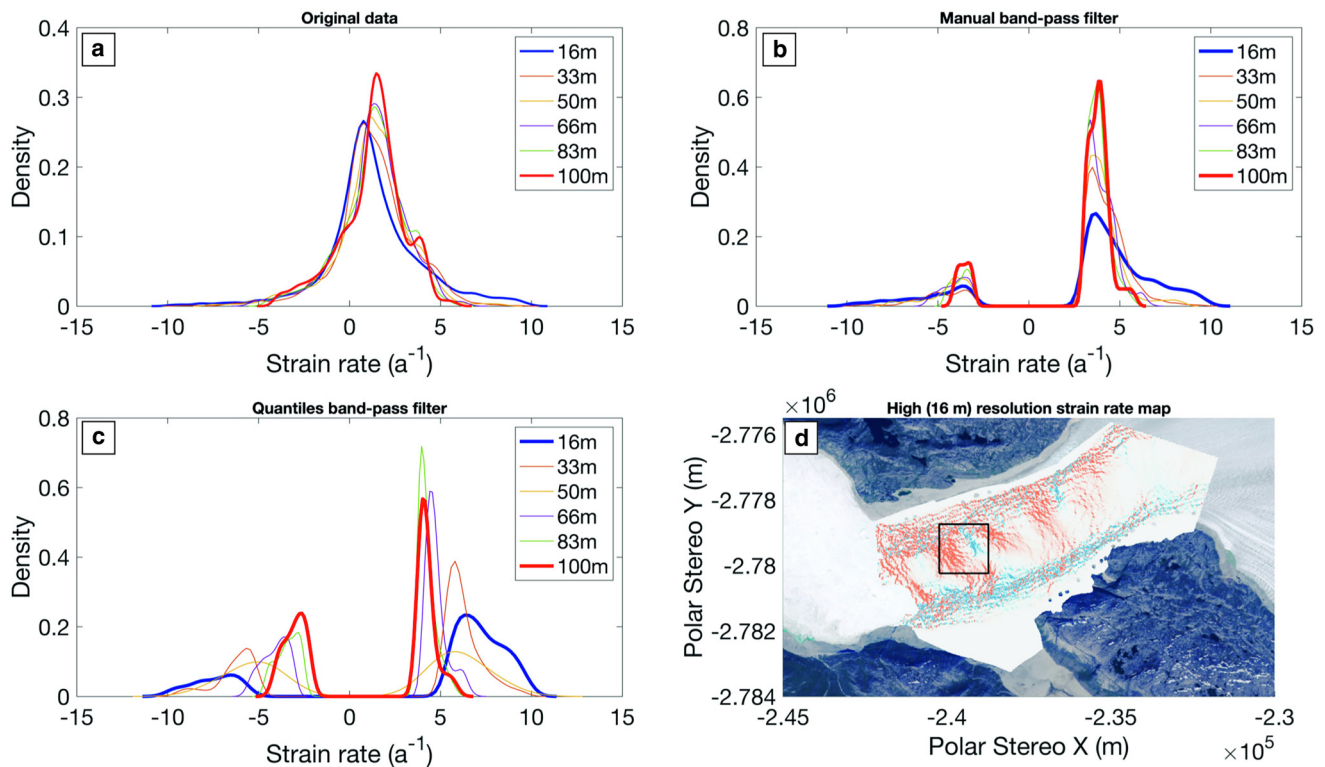
Figure 7. (a) Example of Kernel Density Estimation (KDE) for strain rates at different resolutions (PAZ resolution: 16 m; MEaSUREs resolution = 100 m). (b) KDE plot for strain rates with manually set bandpass filter (−3 to 3) for each data resolution. (c) KDE plot for strain rates with bandpass filter applied based on 25 and 75% quantiles. (d) Overview high-resolution (16 m) strain map with area of interest shown as black square. Basemap showing an ESA Sentinel-2 RGB image acquired on 09/07/2021.

it is likely to be inappropriate to use strain rate extema derived at length scales that match model resolution. Instead, use of sub-grid extreme extensional strain rate values may reduce the level of tuning these parameterisations require to match observations by allowing the application of localised high strain rates and reducing the required tuning of the crevasse water depth parameter. While these sub-grid extrema cannot be applied directly, fine resolution observations of strain rate may be able to provide the basis for a generalised relationship. It is however worth noting that this would likely require a priori assumptions as to the appropriate length scales that both calving and ice damage occur over (Chudley and others, 2021). The results also have implications for strain-rate based calving laws. For example, the higher strain rate ranges derived from high-resolution data suggest that crevasses might reach greater depths than predicted by medium-resolution modelled and observational velocity data. Calving rates determined through crevasse-depth criterion based calving models could therefore require less tuning through the crevasse-water depth parameter (Benn and others, 2007*a*), while tuning parameter values for von Mises-like calving laws may in reality be closer to unity.

In general, the results presented here indicate that currently widely available velocity data does not have the appropriate spatial resolution to either: adequately resolve ice damage or constrain and project calving behaviour on annual to seasonal timescales for strain rate based calving criteria within diagnostic ice sheet models.

Seasonal velocity changes

The seasonal velocity evolution at Narsap Sermia from Stage 1 to 3 is consistent with the findings of previous studies which showed that ice velocities are dependent on the influx of subglacial discharge and the evolution of the subglacial hydrological system

(Sole and others, 2013; Straneo and others, 2013; Motyka and others, 2017; Slater and others, 2019; Davison and others, 2020; Williams and others, 2021). Specifically, Davison and others (2020) found that for the period 2014−2019, flow velocities at Narsap Sermia are characterized by an initial spring acceleration followed by a midsummer slowdown and subsequent recovery to pre-acceleration velocities throughout winter.

However, we find a highly local velocity increase at the northern terminus after the midsummer slowdown, which appears to initiate acceleration across the glacier, and results in overall high velocities throughout winter 2020/21 (Fig. 4, Stage 4). While data gaps at the terminus prevent to determine the spatial extent of the velocity increase in this region, it provides *prima facie* evidence that perturbations at the terminus are able to modulate velocity variations at medium sized, relatively shallow terminating Greenlandic glaciers (Lea and others, 2014*a*, 2014*b*), and not just large, deep terminating glaciers (e.g.(Nick and others, 2009).

The sustained high velocities observed throughout winter 2020/21 indicate a dynamic change in the behaviour of Narsap Sermia as, compared to winter velocities between 2014 and 2019, velocities do not return to pre-spring acceleration magnitudes (Davison and others, 2020). Davison and others (2020) found a similar, yet shorter (1–2 weeks), period of high velocities during January 2019 with air temperatures remaining negative and no runoff present during the period. The longer-term dynamic change found in this study occurs alongside comparatively high air temperatures, which are largely above 0°C until October (Fig. 4d), and no considerable subglacial discharge after mid-September which is consistent with data from previous years (Fig. 4e; Davison and others, 2020). Similar to the brief winter acceleration found by Davison and others (2020), the data presented in this study, does not allow to attribute a distinct driver of neither, the perturbation at the terminus nor the subsequent

sustained high winter velocities in 2020/2021. If, however, increased winter velocities are in fact the result of longer lasting periods of subglacial discharge caused by positive air temperature anomalies, Narsap Sermia could experience increased ice discharge and accelerated retreat in the future through higher winter flow velocities.

High-resolution longitudinal strain and bedrock topography

The analysis of longitudinal strain rates (Fig. 6) shows that over larger spatial scales ($>10^2$ m), strain rates are influenced by changes in bedrock topography and fjord geometry (Bassis and Jacobs, 2013; Enderlin and others, 2013; Catania and others, 2018). A visualisation of flow direction (Fig. S7) shows that downstream of a topographic rise (~7 km from terminus), glacier flow is directed towards the south-southwest, whereas the fjord orientation is towards the southwest. This offset between fjord orientation and flow direction could explain the divergence in observed strain rate patterns between the northern and southern part of the glacier as apparent from Figures 6c and 6e. The results further show, that high longitudinal strain rates are predominantly present in the shallower part of the fjord (depths < 200 m) compared to almost no strain where topography indicates an over-deepened basin (Fig. 6c), which suggests that ice thickness is a control on the influence of bedrock topography on surface dynamics.

Over local spatial scales ($<10^2$ m), the results suggest that strain rates can be related to the underlying bedrock topography, with extensional regimes roughly following local high points (ridges) in the bedrock (e.g. Figure 6c, *i–iv*). These local variations in strain rates driven by topography could promote larger crevasse depths and thus have implications for calving laws as tuning parameters would need to be adjusted to these variations (Benn and others, 2007*a*, 2007*b*; Borstad and others, 2012; Colgan and others, 2016). Past studies have shown that surface dynamics such as crevasse formation can be used to derive information about basal conditions (e.g. Colgan and others, 2016). Thus, strain rates derived from high-resolution velocimetry products could help to better constrain local bedrock topography for shallow grounded glaciers, provided that similar relationship can be found elsewhere (Fastook and others, 1995).

The analysis further revealed an area of compressional strain in southern part of the glacier, located ~1 km from the terminus over a local shallow trough. The compressional zone extends towards the centre of the glacier and extensional strains are present upstream (Figs 6a, h). If this compression zone persists, a perturbation could lead to a change in forces upstream, resulting in increased crevassing and ice damage, as suggested by previous modelling studies (Nick and others, 2009; Lea and others, 2014*b*; Brough and others, 2023). However, as little change is observed over time and data gaps preventing the tracking of the strain rates for most of the study period, the development of this compressional zone remains highly speculative.

The results in this study show that high-resolution velocimetry data have the potential to provide new insights into bedrock topography, however, further research is necessary to establish definitive relationships between surface dynamics, crevasse formation and topography on local scales (e.g. Van Wyk de Vries and others, 2023).

Data availability and transferability

Some long-standing radar satellites, such as TerraSAR-X, Radarsat-2 or COSMO-SkyMed, have the capability to acquire SAR imagery with a high spatial resolution of up to 1 m, however swath widths are small compared to lower resolution modes (Werninghaus, 2004; Staples and Rabus, 2005; Fiorentino and

others, 2016). Newer SAR satellites like PAZ, ICEYE or UMBRA have made use of advances in technology to enable image acquisition with spatial resolutions of up to 0.25 m, yet swath widths remain similar (HDS Team, 2019; Ignatenko and others, 2020; UMBRA, 2024). Most high-resolution data are not freely available so that acquisitions need to be specifically requested or the data has to be commercially acquired, which, over larger spatial scales, requires considerable financial efforts. Therefore, high-resolution SAR data are currently not readily available for most tidewater glaciers in Greenland. While future advances in technology are anticipated to enable image acquisition with ever increasing spatial resolutions, ice-sheet wide high-resolution SAR imagery will most likely not become freely available in the foreseeable future. This might also not be necessary as findings derived from high-resolution data at one tidewater glacier can be transferred to other glaciers with similar characteristics.

For example, the results found in this study could be applied to other medium size, shallow grounded glaciers in Greenland. The observed increase in winter velocities at Narsap Sermia can be used as indicator for larger dynamic changes at tidewater glaciers initiated by a perturbation at the terminus (e.g. Nick and others, 2009). This would be especially relevant for glaciers that experience a midsummer slowdown after spring acceleration (Type 2 glaciers, cf. Moon and others, 2014), and comparatively high air temperatures after the midsummer slowdown.

The determined underestimation of longitudinal strain rate maxima further suggests that surface fracture mechanics (e.g. crevasse formation and depth, ice damage) at other glaciers might differ from what can be derived from medium-resolution data. Taking the findings of this study into account could lead to an improved understanding of the relationship between crevasse depth and calving at other glaciers.

Conclusion

This study presents detailed velocities and strain rates, posted at 16 m for Narsap Sermia derived from high-resolution PAZ spotlight mode SAR data (1 m resolution) for October 2019 to February 2021. These data reveal detailed spatial patterns of strain rate that are of higher magnitude and range than can be derived from medium-resolution data (Fig. 2), with substantial implications for constraining ice flow and calving behaviour of individual tidewater glaciers in ice sheet models. This is because using modelled or observed velocities at medium-resolution (e.g. 100 m) will translate to incorrect derivations of strain rate dependent parameters such as ice damage, crevasse formation rates and depths, and the enhancement factor E. As a result, diagnostic model simulation outputs that use strain rate based calving criteria and do not account for strain rate variability over shorter length scales than present may underestimate mass loss through calving. This is especially relevant for areas where the model resolution is higher than those of the input data.

We further find a spatial pattern of contrasting strain rates between the northern and southern part of the glacier, which appears to be related to a topography forced change in flow direction. This shows that basal topography and fjord geometry play a key role in the sign of strain rates (i.e. extensional or compressional), but current uncertainty around bedrock topography in Greenlandic outlets remains a key challenge to the understanding of this. In addition, the results presented here show that perturbations at the terminus can be a key driver of glacier dynamic change that can propagate upstream at small to medium size Greenlandic tidewater glaciers, which could not have been identified in lower resolution velocity products.

While high-resolution SAR imagery is not available for many tidewater glaciers in Greenland, the result presented here can be

applied to other medium sized, shallow grounded glaciers and thereby provide further insights into their surface dynamics.

References

Amundson JM and 5 others (2010) Ice mélange dynamics and implications for terminus stability, Jakobshavn Isbræ, Greenland. *Journal of Geophysical Research: Earth Surface* **115**(F01005). doi: 10.1029/2009JF001405

Bartholomaus TC and 11 others (2016) Contrasts in the response of adjacent fjords and glaciers to ice-sheet surface melt in West Greenland. *Annals of Glaciology* **57**(73), 25–38. doi: 10.1017/aog.2016.19

Bassis JN and Jacobs S (2013) Diverse calving patterns linked to glacier geometry. *Nature Geoscience* **6**(10), 833–836. doi: 10.1038/ngeo1887

Benn DI, Hulton NRJ and Mottram RH (2007a) 'Calving laws', 'sliding laws' and the stability of tidewater glaciers. *Annals of glaciology* **46**, 123–130. doi: 10.3189/172756407782871161

Benn DI, Warren CR and Mottram RH (2007b) Calving processes and the dynamics of calving glaciers. *Earth-Science Reviews* **82**(3–4), 143–179. doi: 10.1016/j.earscirev.2007.02.002

Borstad CP and 6 others (2012) A damage mechanics assessment of the Larsen B ice shelf prior to collapse: toward a physically-based calving law. *Geophysical Research Letters* **39**(L18502). doi: 10.1029/2012GL053317

Borstad CP, Rignot E, Mouginot J and Schodlok MP (2013) Creep deformation and buttressing capacity of damaged ice shelves: theory and application to Larsen C ice shelf. *The Cryosphere* **7**(6), 1931–1947. doi: 10.5194/tc-7-1931-2013

Brough S, Carr JR, Ross N and Lea JM (2023) Ocean-forcing and glacier-specific factors drive differing glacier response across the 69°N boundary, east Greenland. *Journal of Geophysical Research: Earth Surface* **128**(4), e2022JF006857. doi: 10.1029/2022JF006857

Catania GA and 7 others (2018) Geometric controls on tidewater glacier retreat in central western Greenland. *Journal of Geophysical Research: Earth Surface* **123**(8), 2024–2038. doi: 10.1029/2017JF004499

Choi Y, Morlighem M, Rignot E and Wood M (2021) Ice dynamics will remain a primary driver of Greenland ice sheet mass loss over the next century. *Communications Earth & Environment* **2**(1), 1–9. doi: 10.1038/s43247-021-00092-z

Chudley TR and 7 others (2021) Controls on water storage and drainage in crevasses on the Greenland ice sheet. *Journal of Geophysical Research: Earth Surface* **126**(9), e2021JF006287. doi: 10.1029/2021JF006287

Colgan W and 6 others (2016) Glacier crevasses: observations, models, and mass balance implications. *Reviews of Geophysics* **54**(1), 119–161. doi: 10.1002/2015RG000504

Colosio P, Tedesco M, Fettweis X and Ranzi R (2021) Surface melting over the Greenland ice sheet from enhanced resolution passive microwave brightness temperatures (1979–2019). *The Cryosphere* **15**, 2623–2646. doi: 10.5194/tc-15-2623-2021

Cowton TR, Todd JA and Benn DI (2019) Sensitivity of tidewater glaciers to submarine melting governed by plume locations. *Geophysical Research Letters* **46**(20), 11219–11227. doi: 10.1029/2019GL084215

Davison BJ and 6 others (2020) Subglacial drainage evolution modulates seasonal ice flow variability of three tidewater glaciers in southwest Greenland. *Journal of Geophysical Research: Earth Surface* **125**(9), e2019JF005492. doi: 10.1029/2019JF005492

Enderlin EM, Howat IM and Vieli A (2013) High sensitivity of tidewater outlet glacier dynamics to shape. *The Cryosphere* **7**(3), 1007–1015. doi: 10.5194/tc-7-1007-2013

Fahrner D, Lea JM, Brough S, Mair DWF and Abermann J (2021) Linear response of the Greenland ice sheet's tidewater glacier terminus positions to climate. *Journal of Glaciology* **67**(262), 193–203. doi: 10.1017/jog.2021.13

Fastook JL, Brecher HH and Hughes TJ (1995) Derived bedrock elevations, strain rates and stresses from measured surface elevations and velocities: Jakobshavns Isbræ, Greenland. *Journal of Glaciology* **41**(137), 161–173. doi: 10.3189/S0022143000017858

Fausto R, Van As D and PROMICE Scientific Data (2019) Programme for monitoring of the Greenland ice sheet (PROMICE): automatic weather station data, 2007-present. *Arctic Data Center*. doi: 10.22008/promice/data/aws

Fettweis X and 8 others (2017) Reconstructions of the 1900–2015 Greenland ice sheet surface mass balance using the regional climate MAR model. *The Cryosphere* **11**(2), 1015–1033. doi: 10.5194/tc-11-1015-2017

Fiorentino C, Virelli M and Battagliere ML (2016) COSMO-SkyMed Mission and Products Description. *COSMO-SkyMed-Mission-and-Products-Description_rev3–1. pdf*.

HDS Team (2019) *PAZ Image Product Guide*. HDS Team. Available at https://earth.esa.int/eogateway/documents/20142/37627/PAZ-Image-Products-Guide.pdf

Howat IM, Joughin I, Tulaczyk S and Gogineni S (2005) Rapid retreat and acceleration of Helheim Glacier, east Greenland. *Geophysical Research Letters* **32**(L22502). doi: 10.1029/2005GL024737

Ignatenko V and 5 others (2020) ICEYE Microsatellite SAR Constellation Status Update: Evaluation of first commercial imaging modes. *IGARSS 2020–2020 IEEE International Geoscience and Remote Sensing Symposium.* IEEE, pp. 3581–3584. doi: 10.1109/IGARSS39084.2020.9324531

Joughin I, Kwok R and Fahnestock M (1996) Estimation of ice-sheet motion using satellite radar interferometry: method and error analysis with application to Humboldt Glacier, Greenland. *Journal of Glaciology* **42**(142), 564–575. doi: 10.3189/S0022143000003543

Joughin I and 7 others (2008) Continued evolution of Jakobshavn Isbrae following its rapid speedup. *Journal of Geophysical Research: Earth Surface* **113**(F04006). doi: 10.3189/S0022143000003543

Joughin I, Smith BE, Howat IM, Scambos T and Moon T (2010) Greenland flow variability from ice-sheet-wide velocity mapping. *Journal of Glaciology* **56**(197), 415–430. doi: 10.3189/002214310792447734

Joughin I, Smith BE and Howat IM (2018) A complete map of Greenland ice velocity derived from satellite data collected over 20 years. *Journal of Glaciology* **64**(243), 1–11. doi: 10.1017/jog.2017.73

Joughin I, Howat I, Smith B and Scambos T (2021) MEaSUREs Greenland Ice Velocity: Selected Glacier Site Velocity Maps from InSAR, Version 4. doi: 10.5067/GQZQY2M5507Z

Knight PG (1992) Ice deformation very close to the ice-sheet margin in West Greenland. *Journal of Glaciology* **38**(128), 3–8. doi: 10.3189/S0022143000009539

Larour E, Seroussi H, Morlighem M and Rignot E (2012) Continental scale, high order, high spatial resolution, ice sheet modeling using the Ice Sheet System Model (ISSM). *Journal of Geophysical Research: Earth Surface* **117**(F01022). doi: 10.1029/2011JF002140

Lea JM (2018) The google earth engine digitisation tool (GEEDiT) and the Margin change Quantification Tool (MaQiT)--simple tools for the rapid mapping and quantification of changing Earth surface margins. *Earth Surface Dynamics* **6**(3), 551–561. doi: 10.5194/esurf-6-551-2018

Lea JM and 7 others (2014a) Fluctuations of a Greenlandic tidewater glacier driven by changes in atmospheric forcing: observations and modelling of Kangiata Nunaata Sermia, 1859,--present. *The Cryosphere* **8**, 2031–2045. doi: 10.5194/tc-8-2031-2014

Lea JM and 8 others (2014*b*) Terminus-driven retreat of a major southwest Greenland tidewater glacier during the early 19th century: insights from glacier reconstructions and numerical modelling. *Journal of Glaciology* **60**(220), 333–344. doi: 10.3189/2014JoG13J163

Luckman A and Murray T (2005) Seasonal variation in velocity before retreat of Jakobshavn Isbræ, Greenland. *Geophysical Research Letters* **32**(L08501). doi: 10.1029/2005GL022519

MacGregor JA and 11 others (2016) A synthesis of the basal thermal state of the Greenland Ice Sheet. *Journal of Geophysical Research: Earth Surface* **121**(7), 1328–1350. doi: 10.1002/2015JF003803

Mair D, Nienow P, Sharp M, Wohlleben T and Willis I (2002*b*) Influence of subglacial drainage system evolution on glacier surface motion: Haut Glacier d'Arolla, Switzerland. *Journal of Geophysical Research: Solid Earth* **107**(B8), EPM 8-1–EPM 8-13. doi: 10.1029/2001JB000514

Mair DWF, Sharp MJ and Willis IC (2002*a*) Evidence for basal cavity opening from analysis of surface uplift during a high-velocity event: Haut Glacier d'Arolla, Switzerland. *Journal of Glaciology* **48**(161), 208–216. doi: 10.3189/172756502781831502

Moon T, Joughin I, Smith B and Howat I (2012) 21st-century evolution of Greenland outlet glacier velocities. *Science* **336**(6081), 576–578. doi: 10.1126/science.1219985

Moon T and 6 others (2014) Distinct patterns of seasonal Greenland glacier velocity. *Geophysical Research Letters* **41**(20), 7209–7216. doi: 10.1002/2014GL061836

Moon T, Joughin I and Smith B (2015) Seasonal to multiyear variability of glacier surface velocity, terminus position, and sea ice/ice mélange in northwest Greenland. *Journal of Geophysical Research: Earth Surface* **120**(5), 818–833. doi: 10.1002/2015JF003494

Morlighem M and 6 others (2016) Modeling of Store Gletscher's calving dynamics, West Greenland, in response to ocean thermal forcing. *Geophysical Research Letters* **43**(6), 2659–2666. doi: 10.1002/2016GL067695

Morlighem M and 31 others (2017) Bedmachine v3: complete bed topography and ocean bathymetry mapping of Greenland from multibeam echo sounding combined with mass conservation. *Geophysical Research Letters* **44**, 11051–11061. doi: 10.1002/2017GL074954

Morlighem M and 31 others (2021) IceBridge BedMachine Greenland, Version 4. doi: 10.5067/VLJ5YXKCNGXO

Motyka RJ and 11 others (2017) Asynchronous behavior of outlet glaciers feeding Godthåbsfjord (Nuup Kangerlua) and the triggering of Narsap Sermia's retreat in SW Greenland. *Journal of Glaciology* **63**(238), 288–308. doi: 10.1017/jog.2016.138

Mouginot J and Rignot E (2019) Glacier catchments/basins for the Greenland Ice Sheet. doi: 10.7280/D1WT11

Mouginot J, Rignot E, Millan R, Wood M and Scheuchl B (2019) Annual Ice Velocity of the Greenland Ice Sheet (1972–1990), Dryad, Dataset. doi: 10.7280/D1MM37

Nagler T, Rott H, Hetzenecker M, Wuite J and Potin P (2015) The Sentinel-1 mission: new opportunities for ice sheet observations. *Remote Sensing* **7**(7), 9371–9389. doi: 10.3390/rs70709371

Nick FM, Vieli A, Howat IM and Joughin I (2009) Large-scale changes in Greenland outlet glacier dynamics triggered at the terminus. *Nature Geoscience Letters* **2**(2), 110–114. doi: 10.1038/ngeo394

Riel B, Minchew B and Joughin I (2021) Observing traveling waves in glaciers with remote sensing: new flexible time series methods and application to Sermeq Kujalleq (Jakobshavn Isbræ), Greenland. *The Cryosphere* **15**(1), 407–429. doi: 10.5194/tc-15-407-2021

Rignot E and Kanagaratnam P (2006) Changes in the velocity structure of the Greenland Ice Sheet. *Science* **311**(5763), 986–990. doi: 10.1126/science.1121381

Rohner C and 5 others (2019) Multisensor validation of tidewater glacier flow fields derived from synthetic aperture radar (SAR) intensity tracking. *The Cryosphere* **13**(11), 2953–2975. doi: 10.5194/tc-13-2953-2019

Rosen PA, Gurrola E, Sacco GF and Zebker H (2012) The InSAR scientific computing environment. *EUSAR 2012; 9th European Conference on Synthetic Aperture Radar*, pp. 730–733.

Schoof C (2007) Ice sheet grounding line dynamics: steady states, stability, and hysteresis. *Journal of Geophysical Research: Earth Surface* **112**(F03S28). doi: 10.1029/2006JF000664

Slater DA and 6 others (2019) Estimating Greenland tidewater glacier retreat driven by submarine melting. *The Cryosphere* **13**(9), 2489–2509. doi: 10.5194/tc-13-2489-2019

Sole A and 6 others (2013) Winter motion mediates dynamic response of the Greenland Ice Sheet to warmer summers. *Geophysical Research Letters* **40**(15), 3940–3944. doi: 10.1002/grl.50764

Solgaard A and Kusk A (2019) *Programme for Monitoring of the Greenland Ice Sheet (PROMICE): Greenland Ice Velocity.* Geological survey of Denmark and Greenland (GEUS). doi: 10.22008/PROMICE/DATA/SENTINEL1ICEVELOCITY/GREENLANDICESHEET/V1.0.0

Staples G and Rabus B (2005) RADARSAT-2: Program Overview and Applications. *Anais XII Simpósio Brasileiro de Sensoriamento Remoto, Goiânia, Brasil.* INPE, pp. 4501–4506.

Straneo F and 15 others (2013) Challenges to understanding the dynamic response of Greenland's marine terminating glaciers to oceanic and atmospheric forcing. *Bulletin of the American Meteorological Society* **94**(8), 1131–1144. doi: 10.1175/BAMS-D-12-00100.1

Strozzi T, Luckman A, Murray T, Wegmuller U and Werner CL (2002) Glacier motion estimation using SAR offset-tracking procedures. *IEEE Transactions on Geoscience and Remote Sensing* **40**(11), 2384–2391. doi: 10.1109/TGRS.2002.805079

Studinger M (2014) IceBridge ATM L4 Surface Elevation Rate of Change, Version 1. Greenland. doi: 10.5067/BCW6CI3TXOCY

Sutherland DA and 5 others (2014) Quantifying flow regimes in a Greenland glacial fjord using iceberg drifters. *Geophysical Research Letters* **41**(23), 8411–8420. doi: 10.1002/2014GL062256

Tedstone AJ and 5 others (2015) Decadal slowdown of a land-terminating sector of the Greenland ice sheet despite warming. *Nature* **526**(7575), 692–695. doi: 10.1038/nature15722

UMBRA (2024) *UMBRA Product Guide.* UMBRA. Available at https://help.umbra.space/product-guide

van der Veen CJ (1998) Fracture mechanics approach to penetration of surface crevasses on glaciers. *Cold Regions Science and Technology* **27**(1), 31–47. doi: 10.1016/S0165-232X(97)00022-0

Van Wyk de Vries M, Lea JM and Ashmore DW (2023) Crevasse density, orientation and temporal variability at Narsap Sermia, Greenland. *Journal of Glaciology* **69**(277), 1125–1137. doi: 10.1017/jog.2023.3

Weertman J (1973) Can a water-filled crevasse reach the bottom surface of a glacier. *IASH Publ* **95**, 139–145.

Weidick A (1959) Glacial variations in West Greenland in historical time. Part I. Southwest Greenland. *Bulletin Grønlands Geologiske Undersøgelse* **18**, 1–196. doi: 10.34194/bullggu.v18.6551

Werninghaus R (2004) TerraSAR-X mission. *SAR image analysis, modeling, and techniques VI.* SPIE, pp. 9–16. doi: 10.1117/12.511500

Williams JJ, Gourmelen N and Nienow P (2021) Complex multi-decadal ice dynamical change inland of marine-terminating glaciers on the Greenland Ice Sheet. *Journal of Glaciology* **67**(265), 833–846. doi: 10.1017/jog.2021.31